Micromechanical analysis of UD CFRP composite lamina under multiaxial loading with different loading paths

Jiayun Chen [1, 2,*], Lei Wan [1,*], Yaser Ismail [3], Pengfei Hou [2], Jianqiao Ye [4], Dongmin Yang [1,†]

[1] Institute for Materials and Processes, School of Engineering, University of Edinburgh EH9 3FB, Edinburgh, UK
[2] College of Mechanical and Vehicle Engineering, Hunan University, Changsha 410082, PR China
[3] Groundforce Shorco, Gildersome, Leeds LS27 7HJ, UK
[4] Department of Engineering, Lancaster University, Lancaster LA1 4YW, UK

Abstract

The influences of loading path on the failure of unidirectional (UD) carbon fibre reinforced polymer (CFRP) composite laminae IM7/8552 are studied in this study. A 3D representative volume element (RVE) based micromechanical model is established using finite element method (FEM) to capture the coupled effects of fibres, matrix and fibre/matrix interface on the failure under different multiaxial loading conditions. An artificial neural network (ANN) is adopted to identify experimentally difficult-to-measure micro-parameters of interface, such as interface thickness and stiffnesses, for the construction of the high-fidelity RVE. In order to precisely control the loading path with the consideration of Poisson's effects, the RVE is loaded by force at the dummy points instead of using the commonly used displacement loading approach. Three different loading paths are compared in each case, and the results show that the failure strength and patterns of the RVE under combined transverse and out-of-plane compressions as well as in-plane shear are independent of loading paths.

Keyword:

Loading path; Failure prediction; CFRP; RVE; FEM

1. Introduction

Due to the lightweight, design flexibility, corrosion resistance, high stiffness and strength and other advantages, composite materials are widely applied in aerospace, automotive, wind energy and even biomedical engineering, etc [1–3]. In order to accelerate the design process of new composite products, reliable and accurate failure criteria for composites have been sought after. For decades, many attempts have been made to propose an explicit mathematic form of failure criteria for composites [4–10]. All those studies assume the failure surface is determined, which means the failure is independent of loading path. It is generally accepted that when an isotropic material remains elastic before failure, its failure points are independent of loading path [11], because whatever the loading path is, the energy accumulated for failure is the same. However, differing from the isotropic materials, carbon fibre reinforced polymer (CFRP) composites consist of at least two phases, i.e., fibre and matrix. Although carbon fibres may remain elastic prior to failure, the polymer matrix tends to show extensive plasticity after the yielding point, especially subjected to compression and shear loadings [12]. Besides, the failure mode of the composites varies under different loading conditions, including fibre breakage, interface debonding, matrix cracking and interlaminar delamination [13]. Therefore, it is vital to understand the

* These two authors contribute equally.

† Corresponding author. Email: Dongmin.Yang@ed.ac.uk

effects of loading paths on the failure strength and failure modes of composite materials under different loading conditions.

Controlling the loading path with current experimental devices remains challenging. The common tests for studying the mechanical response of composites under in-plane shear and transverse tension/compression are the off-axis tensile/compressive tests [14,15] and the Arcan tests [16,17], where the ratio of stress components is always kept same throughout each test. Alternatively, thin-walled tubes loaded by axial/torsional testing facility can provide the same loading conditions, but the initial defect, buckling and slitting could introduce discrepancy or even errors in the experimental results [18]. For samples under biaxial transverse tension/compression, a biaxial linkage [19] can be used on a uniaxial testing machine. In the case of triaxial loading tests, Welsh and Adams [20] designed an electromechanical triaxial test facility, which can achieve any stress ratio in the triaxial stress space (σ_1, σ_2, σ_3). An alternative method is to use the high-pressure facility, in which the triaxial stress space (τ_{12}, σ_1=σ_2=σ_3) [21,22] or (σ_1, σ_2=σ_3) [23,24] can be realised. However, these tests can only provide a single loading path, which is either radial or pseudo-radial. So as to compare the mechanical response of composites under different loading paths, other efforts have been made in previous works. Choo [18] used a thin wall hoop wound tubes loaded by servo-hydraulic feed-back controlled multiaxial test rig to compare the failure points in stress space (+σ_1, -σ_2) and (-σ_2, τ_{12}) with two loading paths. They found that the failure points are independent of loading path for fibre fracture mode. However, in some cases, the loading path can influence the failure points in matrix fracture mode. Vogler and Kyriakides [25] compared the failure points for two different loading paths under in-plane shear and transverse compression on a biaxial test machine, and the results suggested that the loading paths have negligible influences on the failure points of composites under such loading condition. Due to limited loading paths or stress ratios used in experiments, numerical methods have been adopted in some studies, such as the FE-based RVE. RVE is the minimal material volume that contains statistically sufficient mechanisms of deformation processes [26], and RVE method is a widely accepted tool to study the failure process of composite materials beside the extended finite element (XFEM) [27,28] and the phase field model (PFM) [29-32]. Totry, Gonzalez and LLorca [11] used a 2D RVE to predict the failure points of a composite laminae under transverse compression and out-of-plane shear, and they found that the loading paths (pseudo-radial and orthogonal path) show no effect on the failure locus. Sun et al. [33] used a 3D RVE to predict the failure points of a composite lamina under combined transverse compression and out-of-plane/in-plane shear biaxial loading, and the results also suggested the failure points are independent of the loading paths. In this work, the same stress space (-σ_2, τ_{12}) was considered. However, another two stress combinations of (-σ_2, -σ_3) and (-σ_2, -σ_3, τ_{12}) are also included in this study, together with three different loading paths, namely radial, orthogonal and zigzag loading paths.

In the aforementioned works using experimental methods and/or numerical methods, only some biaxial loading cases were investigated. However, the effect of loading paths on failure points in other different biaxial and triaxial loading cases are still unknown. In view of this, this paper adopts a 3D RVE to compare the failure points of composite laminae in stress spaces of (-σ_2, -σ_3), (-σ_2, τ_{12}) and (-σ_2, -σ_3, τ_{12}) obtained from different loading paths. In addition, the RVE in this paper consists of three phases of materials, including fibres, matrix and non-zero interface. Periodical boundary condition (PBC) is adopted for the micromechanical analysis to ensure the RVE maintains reliable homogenised macroscale properties [34]. In order to allow direct control of the loading paths, the RVE is loaded by a force loading approach instead of the commonly used displacement loading. Furthermore, previous studies only discussed the monotonic loading path, but in reality, the path of loadings upon the composite during its service loading lifetime is much more complex. Therefore, this study introduces a more complex loading path called zigzag loading path in addition to the radial and orthogonal loading paths, in which the new loading path can introduce extra plastic strain during the loading conditions.

At last, this paper is organised in the following structure. In Section 2, the methodology is introduced, including details of the RVE, periodic boundary conditions and loading paths. In Section 3, the failure strength and failure patterns of RVE under uniaxial loading, biaxial loading and triaxial loading with three different loading paths are compared and discussed. At last, conclusion is presented in Section 4.

2. Methodology

2.1 RVE based micromechanical FE model

The computational micromechanical FE model is based on an RVE including random dispersion of parallel carbon fibres and polymer matrix, which represents a slice of a UD composite laminae with certain thickness in the transversal direction. It was found that 50 fibres with a RVE are enough to adequately capture the characteristics of the material microstructure with reasonable computing time [35]. Moreover, the average diameter of fibres and their volume fraction within a specific RVE are acquired as 7 mm and 60% from experiments, respectively [36]. A discrete element method-based approach, combining experimental data and an initial periodic shaking model, is adopted for the generation of fibres random distribution in two dimensions [37]. The 3D RVE model of the UD laminae is achieved by extruding the 2D model along its fibre direction. The microstructure of the RVE is idealised as the dispersion of circular fibres randomly distributed in the matrix. The RVE thickness is set to 1 μm in this study which is selected as a compromise between the numerical simulations speed and the aspect ratio of the FE mesh, resulting in the size of the RVE to be 50 μm×50 μm×10 μm. An identified interface thickness using an artificial neural network is utilised in the construction of the 3D RVE model, which will be described in detail in Section 2.2.

Fibres and matrix in the RVE model are discretised with eight-node reduced hexahedral elements (C3D8R) and six-node wedge elements (C3D6), while the interface is meshed with first-order cohesive elements (COH3D8), which can be found in in

. Here in this study, the Abaqus/Explicit is used to construct the FE model considering the convergence issue when damage within the RVE occurs. Moreover, a cohesive zone model [38-41], which considers the friction between fibres and matrix after the interface fails, will be implemented into the FE model using VUMAT, together with the Coulomb friction law in our further work, where around 50,000 elements are used to balance the result accuracy and computational cost. Periodic mesh is achieved so that every node has identical counterparts on the opposite faces regarding plane coordinates to apply periodic boundary conditions (PBC). Mass scaling is utilised to accelerate the numerical simulations within the scheme of ABAQUS/Explicit. A ratio of the kinetic energy over the internal energy of the system is monitored to determine whether the mass scaling has any significant influence on the numerical results. The time increment is chosen as 6×10^{-6} s in this study, so that the ratio is calculated below 10%, suggesting the mass scaling has insignificant influence on the simulated results [33].

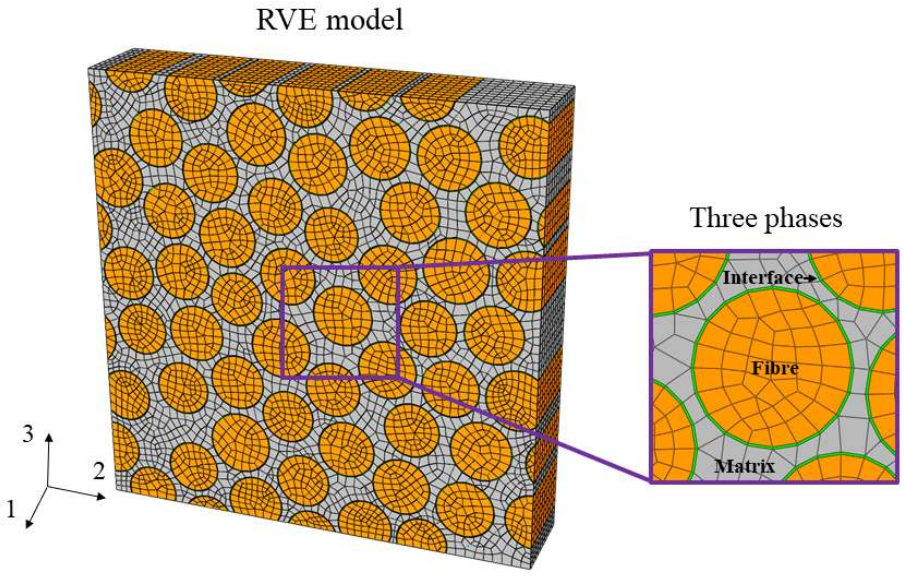

Fig 1. Schematic of the three-phase based 3D RVE FE model.

2.2 Constitutive and damage models of constituents

Carbon fibres are modelled as transversely isotropic and linear materials, and their material properties are found in Table 1. The polymer in this study is modelled as an isotropic elasto-plastic solid. It was found that the hydrostatic stress has significant influences on the mechanical behaviour of polymers [42], in which two different behaviours were observed experimentally, such as brittle fractures under tension while and large plasticity under compression and shear [43]. These characteristics of polymer are taken in to consideration in the failure analysis of composite materials under multiaxial stress states, with the extended Drucker-Prager (D-P) yield model associated with a ductile damage criterion [44], the modified Drucker-Prager plastic damage model [45] and the elasto-plastic with isotropic damage constitutive model proposed by Melro et al. [46]. In order to generate numerical data from the RVE model efficiently and to avoid changing hardening pattern manually in the extended D-P model at the damage mode transition point under biaxial loadings [44], the ABQUS built-in modified D-P plastic damage model is adopted. The constitutive model is combined the yield function proposed by Lubliner et al. [47] with modifications accounting for damage evolution subjected to tensile and compressive loads [48]. The yield surface of the epoxy is expressed by a modification of the Drucker–Prager yield function according to,

$$\Phi\left(I_1, J_2, \sigma_I, \beta, \alpha\right) = \frac{1}{1-\alpha}\left(\sqrt{3J_2} + \alpha I_1 + B\left\langle \sigma_I \right\rangle\right) - \sigma_{myc} = 0, \tag{1}$$

where I_1 is the first invariant of stress tensors, J_2 the second invariant of deviatoric stress tensors, α the pressure-sensitivity parameter of the Drucker-Prager yield criterion, σ_I the maximum principal stress, $<>$ the Macaulay brackets and it returns the argument if it is positive and zero otherwise, and B a function of the tensile and compressive yield stresses (σ_{myt} and σ_{myc}), which can be defined as,

$$B = \frac{\sigma_{myt}}{\sigma_{myc}}(1-\alpha) - (1+\alpha), \tag{2}$$

wherein α can be determined according to $\tan\beta = 3\alpha$ from the internal friction angle of the material (β), which controls the hydrostatic pressure dependence of the plastic behaviour of the material.

After onset of damage under tensile loads, the quasi-brittle behaviour of the polymer is controlled by an exponential cohesive law, characterised by a single normalized scalar damage variable. While for the behaviour of matrix under uniaxial compressive loads, plastic hardening is considered by using the experimentally obtained stress-strain data, associated with a damage model, which is illustrated in Fig. 2(a). Readers can refer to [45] for more details of the constitutive model.

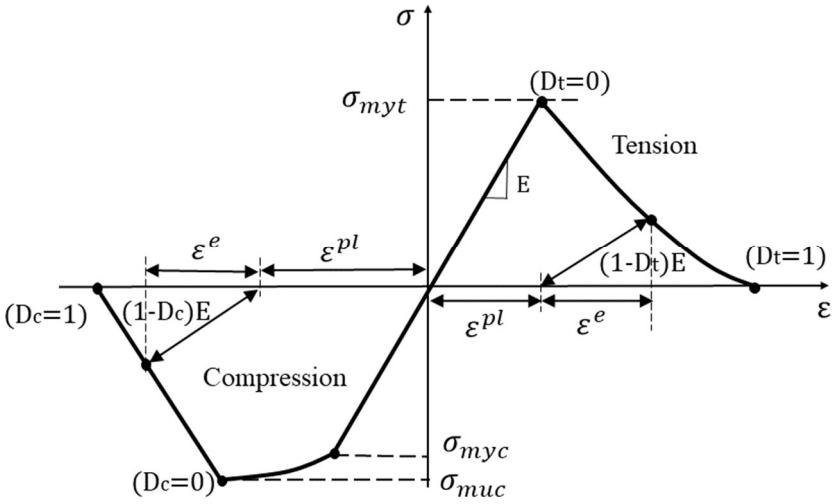

Fig 2. Schematic of the modified Drucker-Prager damage-plastic model for the epoxy matrix.

The interface is modelled with bilinear traction-separation law based cohesive elements, see Fig. 3(a). The linear elastic behaviour of the cohesive elements is controlled by a large penalty stiffness K to ensure displacement continuity while avoiding convergence difficulties. Because there is lack of experimental data for the stiffness of fibre/matrix interface, in most case the empirical values (i.e., 10^4 GPa/mm-10^5 GPa/mm) are adopted [33,45,49,50]. However, in order to obtain more reasonable and specific interface stiffnesses for the IM7/8552 composite lamina, parameter identification of these stiffnesses is conducted with an inverse method described in Section 2.3.

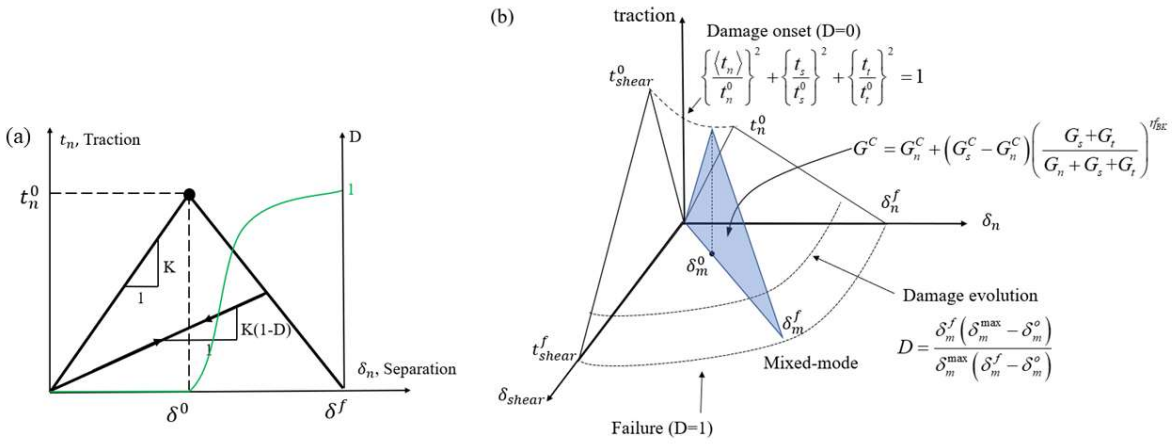

Fig 3. Schematic of the traction-separation cohesive law of the interface: (a) uniaxial tension in normal direction associated with the damage parameter and (b) representation of a mixed-mode damage evolution.

The interface is modelled using cohesive elements, which are governed by the bilinear traction-separation law. The separations are denoted by $< \delta_n >, \delta_s, \delta_t$ for the normal and two shear directions, respectively. The Macaulay bracket (< >) represents that a pure compressive stress state does not initiate damage. The original thickness of the element is denoted by T_0. Therefore, the nominal strains are expressed as

$$\varepsilon_n = \frac{<\delta_n>}{T_0}, \varepsilon_s = \frac{\delta_s}{T_0}, \varepsilon_t = \frac{\delta_t}{T_0}, \tag{3}$$

Then the elastic behaviour of the cohesive elements can be written as follow,

$$\begin{Bmatrix} t_n \\ t_s \\ t_t \end{Bmatrix} = \begin{bmatrix} \mathrm{K}_{nn} & \mathrm{K}_{ns} & \mathrm{K}_{nt} \\ \mathrm{K}_{ns} & \mathrm{K}_{ss} & \mathrm{K}_{st} \\ \mathrm{K}_{nt} & \mathrm{K}_{st} & \mathrm{K}_{tt} \end{bmatrix} \begin{Bmatrix} \delta_n \\ \delta_s \\ \delta_t \end{Bmatrix} = \mathbf{K}\varepsilon, \tag{4}$$

where $t_i \ (i = n, s, t)$ represent the nominal traction stress in the normal and two shear directions. Uncoupled behaviour between the normal and shear components is considered for simplicity so that the off-diagonal terms in this matrix are set to be zero and two shear stiffnesses are assumed to be same.

A quadratic failure criterion is chosen for the determination of the damage onset of the cohesive elements, and the damage occurs when the criterion involving the sum of nominal stress ratios reaches 1. The criterion is represented as

$$\left\{\frac{\langle t_n \rangle}{t_n^0}\right\}^2 + \left\{\frac{t_s}{t_s^0}\right\}^2 + \left\{\frac{t_t}{t_t^0}\right\}^2 = 1, \tag{5}$$

where t_n^0, t_s^0 and t_t^0 represent the interface strengths in the normal and two shear directions. Damage evolution is defined based on the traction separation law, and the dissipated fracture energy is used to determine the separation displacement at failure.

After the damage initiation, the traction stress $t_i \ (i = n, s, t)$ starts to decrease according to $t_i = (1 - D) \ t_i^0 \ (i = n, s, t)$, and the degradation factor *D* is controlled by

$$D = \frac{\delta_m^f \left(\delta_m^{\max} - \delta_m^o\right)}{\delta_m^{\max} \left(\delta_m^f - \delta_m^o\right)}, \tag{6}$$

D monotonically increases from 0 (at damage onset) to 1 (at final failure), see Fig. 3. To describe the evolution of damage of interface under combined normal and shear loadings, the effective displacement δ_m is introduced as $\delta_m = \sqrt{< \delta_n >^2 + \delta_s^2 + \delta_t^2}$. Therefore, δ_m^f is the effective separation at complete failure, which is calculated from the fracture energy G^C dissipated due to the mix-mode failure, $\delta_m^f = 2G^C / T_{eff}^0$, where the T_{eff}^0 represents the effective traction at damage initiation. δ_m^0 is the effective separation at damage initiation, and δ_m^{max} refers to the maximum value of the effective separation attained during the loading history.

The Benzeggath-Kenane criterion is adopted to the fracture energy dissipation during the damage propagation of the cohesive elements. The criterion reads,

$$G^C = G_n^C + \left(G_s^C - G_n^C\right)\left(\frac{G_s + G_t}{G_n + G_s + G_t}\right)^{\eta_{BK}^c}, \tag{7}$$

where η_{BK}^{C} is the BK power exponent, G_n^C and G_s^C are the critical fracture energy release rates in the normal and shear directions, respectively. And G_n, G_s and G_t are the reciprocal work under mixed mode propagation. The response of the cohesive constitutive model under normal, shear and mixed mode conditions can be found in Fig. 3(b). Due to the restriction of experimental approaches, the critical energy release rate of the interface between fibres and matrix in normal mode, G_n^C, cannot be measured so it is usually assumed between 2–5 J/m^2 [45,46,51]. Therefore, in this study, the energy of 2 J/m^2 is adopted in the simulations. Besides, because there is no experimental data for interface fracture energies in the shear modes of uniaxial laminae IM7/8552, they are set equal to the cracking fracture energy of matrix, 100 J/m^2, which is similar to the one used in [45,52]. More details of this cohesive zone model and its numerical implementation can be found in [44]. It should be noted that in this model, the friction between fibres and matrix after interface failure has not yet been considered in the element based cohesive zone model, although it shows large effects on the shear hardening under the moderate compressive stress. It has insignificant influences upon the failure points of the RVE under multiaxial loads since the interface failure does not occur under the moderate compressive stress in all three loading paths until the RVE is approaching its final failure.

2.3 The identification of the interface micro-parameters

Considering the influences of difficult-to-measure experimentally interface micro-parameters on the failure mechanisms of composites, more reliable data are necessarily required. Therefore, an inverse method using artificial neural network (ANN), which is proposed in previous our work [53], is adopted for the uncertainty identification. First, 1,000 samples are generated, each including different micro-parameters and corresponding macro-parameters. The micro-parameters are generated with Latin hypercube sampling and the corresponding macro-parameters are calculated by ABAQUS, as illustrated in Fig 4. Then, samples are used to train an ANN model, of which 80% are used as training set, 10% are used as validation set and 10% are used as test set. As shown in Fig 5, the ANN model is built on the open-source platform TensorFlow 2.1.0, including an input layer, two hidden layers and an output layer. There are 8 neurons in the input layer representing the 8 micro-parameters, 6 neurons in both hidden layers, and 5 neurons in the output layer representing the 5 macro-parameters. Specifically, the sigmoid function is chosen as the activation function for the hidden layers, and the linear function is chosen as activation function for the output layer. Furthermore, binary cross entropy loss function, combined with Nadam optimisation algorithm [54], is used for training the ANN model, and L2 regularisation was adopted for preventing overfitting. After training, the mean squared errors of training set and test set are as low as 0.0034 and 0.0044, which proves that this ANN model reaches a high accuracy for predicting macro-parameters from micro-parameters.

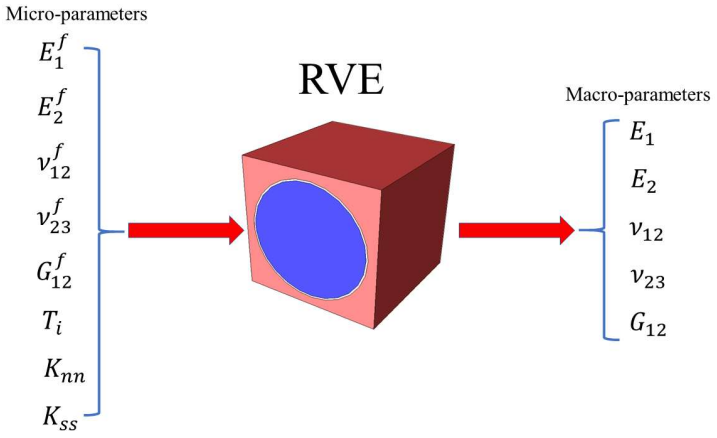

Fig 4. Micro-parameters (Young's modulus E_1^f, E_2^f, Possion's ratio υ_{12}^f, υ_{23}^f shear modulus G_{12}^f, of fibre, the thickness T_i and stiffness K_{nn}, K_{ss} of interface) and macro-parameters (Young's modulus E_1 , E_2 , Poisson's ratio υ_{12}, υ_{23} shear modulus G_{12}, of UD laminae)

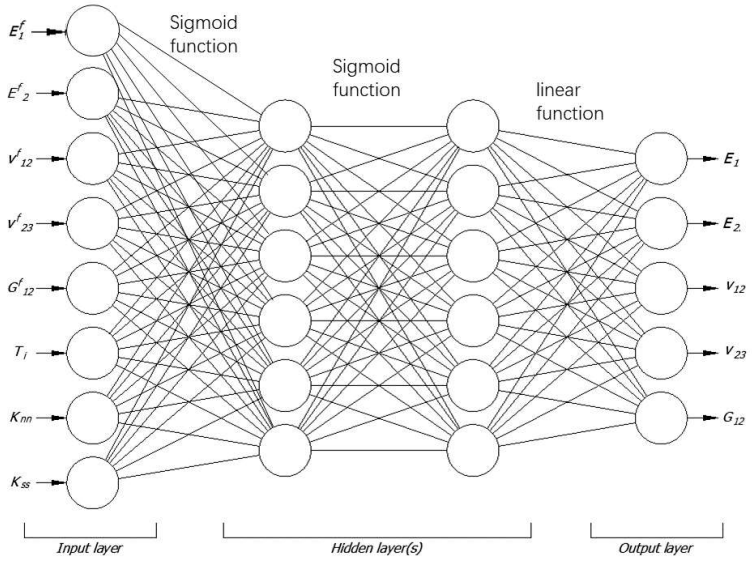

Fig 5. ANN scheme for fibre and interphase parameters identification

Then, another 1,000,000 samples are generated by Latin hypercube sampling with the trained ANN model. The sample with the highest similarity of macro-parameters compared to the experimental data of the target material (IM7/8552 composite) is selected based on Eq. (8). The micro-parameters of the selected sample are input into the RVE model in order to predict the five macro-parameters. The comparison between the experimental data, ANN and RVE predictions can be found in Table 1, which shows excellent agreement between the ANN and RVE predictions and the experimental data. Therefore, the experimentally difficult-to-measure micro-parameters are identified for the high-fidelity FE RVE model with randomly distributed fibre distributions and non-zero thickness interface.

The similarity between the macro-parameters of generated samples and material properties of a unidirectional lamina of IM7/8552 composite materials is defined by the Euclidean distance function, as below:

$$F(sample)=\sqrt{\left(\frac{E_1^s}{E_1}-1\right)^2+\left(\frac{E_2^s}{E_2}-1\right)^2+\left(\frac{\nu_{12}^s}{\nu_{12}}-1\right)^2+\left(\frac{\nu_{23}^s}{\nu_{23}}-1\right)^2+\left(\frac{G_{12}^s}{G_{12}}-1\right)^2}\,, \tag{8}$$

where E_1^s and E_2^s are the predicted longitudinal and transverse modulus, ν_{12}^s and ν_{23}^s are the predicted Possion's ratio and G_{12}^s is the predicted shear modulus. E_1, E_2, ν_{12}, ν_{23} and G_{12} are the material properties of uniaxial lamina IM7/8552. The material properties and identified parameters can be found in Table 1.

Table 1. Material properties of the IM7 fibre and 8552 epoxy, interface parameters and the uniaxial laminae IM7/8552. [36,52,55]

IM7 fibre properties						
	$E_1^f\,(\mathrm{GPa})$	$E_2^f=E_3^f\,(\mathrm{GPa})$	ν_{12}^f	ν_{23}^f	$G_{12}^f\,(\mathrm{GPa})$	$G_{23}^f\,(\mathrm{GPa})$
	287	13.40	0.29	0.48	23.8	7
8552 epoxy properties						
	$E_m\,(\mathrm{GPa})$	ν_m	$\sigma_{myt}\,(\mathrm{MPa})$	$\sigma_{myc}\,(\mathrm{MPa})$	$G_m\,(\mathrm{J/m^2})$	
	4.08	0.38	99	130	100	
Interface properties						
	Thickness (mm)	K_{nn} (GPa/mm)	$K_{ss}=K_{tt}$ (GPa/mm)	t_n^0 (MPa)	$t_s^0=t_t^0$ (MPa)	G_n^C $(\mathrm{J/m^2})$	$G_s^C=G_t^C$ $(\mathrm{J/m^2})$
	0.0001	253	682	58	92	2	100
Uniaxial laminae IM7/8552						
	$E_1\,(\mathrm{GPa})$	$E_2=E_3\,(\mathrm{GPa})$	ν_{12}	ν_{23}	$G_{12}\,(\mathrm{GPa})$	
Experiment	162.95	9.0	0.32	0.5	5.17	
Selected sample-ANN	163.0	8.98	0.32	0.5	5.0	
Selected sample-RVE	163.21	8.99	0.32	0.5	5.0	

2.4 Periodic boundary conditions and loading approaches

When an RVE is constructed, periodic boundary conditions (PBCs) [56,57] are necessary to ensure the periodic displacement and traction fields of outside of RVE by introducing identical relative displacement between the nodes of two corresponding surfaces, and the value of the relative displacement could be positive or negative. The unified PBCs are generally written with displacement vectors $\overrightarrow{U_1}$, $\overrightarrow{U_2}$ and $\overrightarrow{U_3}$, as below:

$$\begin{cases} \vec{u}\left(0,x_2,x_3\right)-\vec{u}\left(L_1,x_2,x_3\right)=\overrightarrow{U_1} \\ \vec{u}\left(x_1,0,x_3\right)-\vec{u}\left(x_1,L_2,x_3\right)=\overrightarrow{U_2} \\ \vec{u}\left(x_1,x_2,0\right)-\vec{u}\left(x_1,x_2,L_3\right)=\overrightarrow{U_3} \end{cases}, \tag{9}$$

where L_1 (i=1, 2, 3) is the length of the RVE, and $\overrightarrow{U_i}$ (i=1, 2, 3) are the relative displacement between two nodes on the pair of opposite surfaces. Three dummy points are introduced to apply the load, such that it is easy to achieve various loading conditions with only modifications of displacements of these nodes. Here in this study, the relative formulation [56] is used for constructing the equations of periodic boundary conditions, where the vertex A and three edges AE, AB and AD are selected as the local coordinate system. The full set of equations to apply PBCs are demonstrated on the one fibre unit cell in Fig 6 (a) and written in Table 2, which constrain all the surfaces, edges and vertices of the RVE, where $\hat{u}_i^j (i=1,2,3; j=1,2,3;$ i is the main direction and j is the label of dummy points) is the displacement of dummy points. Thus, macro-strains ε_{ij} can be defined by the displacement and the corresponding dimensions L_i (i=1, 2, 3).

$$\varepsilon_{ij}=\frac{\hat{u}_j^i}{L_i}, \tag{10}$$

The equations are sorted in three groups: (i) internal nodes of the surfaces; (ii) nodes at the edges except vertices and (iii) vertices. The details of PBC and its implementation in the RVE modelling can refer to [44,56]. A schematic of the RVE with PBCs is shown in Fig 6 (b), where the fibres on the edges are distributed periodically while the fibres inside are distributed randomly.

Table 2. Equations in the form of relative formulation for PBCs

Surfaces	Edges	Vertices
$u_i^{DHGC}-u_i^{AEFB}=\hat{u}_i^3$	$u_i^{DH}-u_i^{AE}=\hat{u}_i^3$	$u_i^{D}-u_i^{A}=\hat{u}_i^3$
	$u_i^{HG}-u_i^{EF}=\hat{u}_i^3$	$u_i^{H}-u_i^{E}=\hat{u}_i^3$
	$u_i^{CG}-u_i^{BF}=\hat{u}_i^3$	$u_i^{G}-u_i^{F}=\hat{u}_i^3$
	$u_i^{CD}-u_i^{AB}=\hat{u}_i^3$	$u_i^{C}-u_i^{B}=\hat{u}_i^3$
$u_i^{BCGF}-u_i^{ADHE}=\hat{u}_i^2$	$u_i^{BC}-u_i^{AD}=\hat{u}_i^2$	$u_i^{B}-u_i^{A}=\hat{u}_i^2$
	$u_i^{FG}-u_i^{EH}=\hat{u}_i^2$	$u_i^{F}-u_i^{E}=\hat{u}_i^2$
	$u_i^{BF}-u_i^{AE}=\hat{u}_i^2$	
$u_i^{EFGH}-u_i^{ABCD}=\hat{u}_i^1$	$u_i^{EF}-u_i^{AB}=\hat{u}_i^1$	$u_i^{E}-u_i^{A}=\hat{u}_i^1$
	$u_i^{EH}-u_i^{AD}=\hat{u}_i^1$	

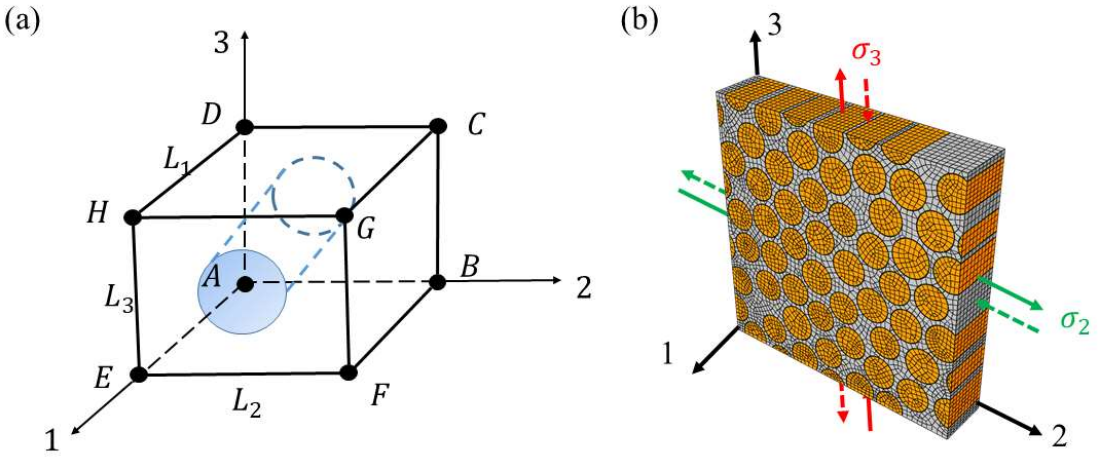

Fig 6. (a) Unit cell for the interpretation of PBCs and (b) Schematic of the RVE with fibres.

In the work conducted by Sun et al. [33], the displacement loading method were adopted to control the loading path in the stress space σ_2-τ_{23}. However, due to the Poisson's effect, it is tricky to control the loading path in the stress space σ_2-σ_3. In the stress space σ_2-τ_{12}, an orthogonal path can be realised by implementing the out-of-plane normal strain ε_3 and transverse normal strain ε_2 in sequence, see in Fig 7 (a). But in the stress space σ_2-σ_3, when the second displacement load is implemented, the second segment of loading path will slope. For example, when an orthogonal loading path is chosen, in which σ_2 is the first segment and σ_3 is second segment by means of the displacement loading. When RVE is loaded with ε_3, the resultant ε_2 should change accordingly due to the Poisson effect, however, the strain ε_2 is fixed in the second step when the σ_3 is loaded, resulting in a higher resultant, uncontrollable σ_2, as shown in Fig 7 (b).

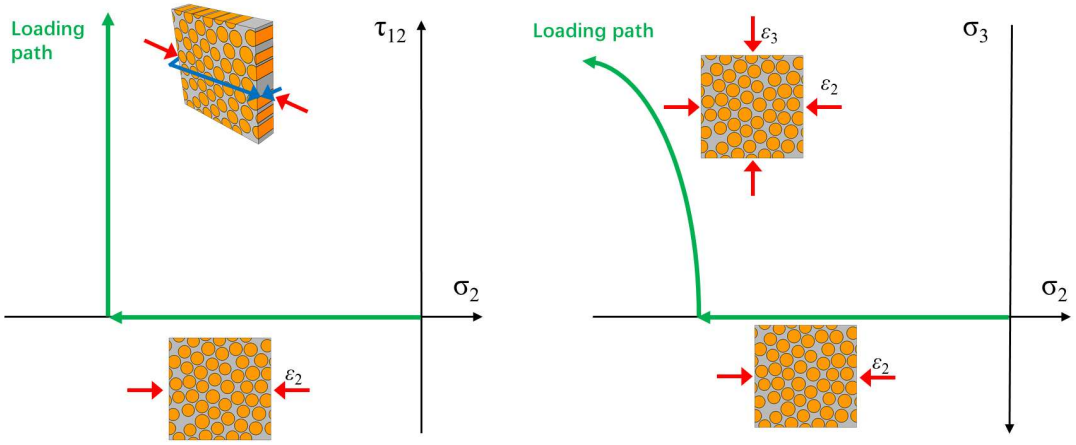

Fig 7. Loading paths for the RVE with displacement loading

In this case, the force loading method [56, 57] is used in this paper, in which the macro-stress σ_{ii} can be controlled by the concentrated forces F_i at the dummy points,

$$\sigma_{ij} = \frac{F_i}{A_j}, \tag{11}$$

where A_j is the area of surface subjected by loads. Besides, because the force loading method does not constrain the displacement of boundary, the Poisson's effect can be involved in deformation.

2.5 Loading paths

Three different loading paths are considered in this paper, namely the radial path, the orthogonal path and the zigzag path, which are illustrated in a 2D case (σ_i-σ_j) in Fig 8. The radial path is most commonly used in experiments, in which all loads increase simultaneously with a certain displacement ratio until the failure occurs, such that the failure point can be obtained. The orthogonal loading path is adopted in this study to investigate the absence of stress coupling which exists in the radial loading path on the determination of failure point. In the orthogonal loading path, the stresses (converted from equivalent loads applied on the dummy points) are applied to the surfaces of the RVE in two sequential steps. The first stress increases from zero until the corresponding component of the failure point obtained in the radial path, and remains constant; then the second stress increases from zero until the RVE fails, such that the orthogonal path and its failure point can be determined. The zigzag path is designed to study the effect of extra plastic deformation on the failure points, and this is highly likely in real working condition for composite. In this loading path, the first applied stress reaches region between the failure point of the RVE with uniaxial loading and the failure point in radial path, which bring extra plastic deformation for this case and then decreases, in the meantime the second stress increases simultaneously at a specific ratio to ensure the loading path passes through the failure point obtained from the radial loading path, such that the zigzag path and its failure point can be obtained.

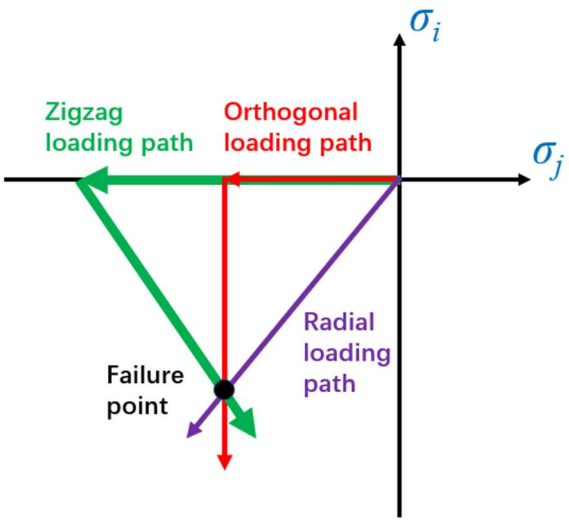

Fig 8. Three loading paths in 2D σ_i-σ_j case

3. Verification of the force loading method

In this section, numerical results of the RVE subjected to uniaxial force and displacement loads are presented to verify the equivalence between the force loading method and the displacement loading method for the RVE. Besides, different from the displacement loading, in which the failure point can be clearly determined when the resultant stress drops, the applied stress in the force loading method increases monotonically. Therefore, the commonly used approach in the displacement loading to determine the failure point when the resultant stress drops cannot be directly used in the force loading method. Here in this study, a new approach is proposed to determine the failure point of the RVE subjected to force loadings.

The stress-strain and stress-energy curves for the RVE under transverse compression stress σ_2 or in-plane shear stress τ_{12}, defined in Eq. (10) and Eq. (11), using both displacement and force loading methods are shown in Fig 9 and Fig 11, respectively. It is found that when the RVE is applied with displacement loading, the stress witnesses a reduction when it reaches the peak value at the failure point. Besides, the stress-strain curves of two loading methods are in good agreement before failure point, but for displacement loading method, some fluctuations can be observed before the peak. This is because that the matrix in some regions fails and enters into a soften stage before final failure of the RVE, resulting in the fluctuation of macro-stress in the stress-strain curves. However, no such reduction can be observed in the RVE applied by force loading, which is due to the fact that the applied stress is controlled by force loading directly. In order to identify the failure point of the RVE with force loading, the kinetic energy is considered. When the RVE is loaded with forces, the force loading can surpass the load carried by the RVE at failure, such that extra work due to the failure transfers into the kinetic energy, which can result in a dramatic growth of kinetic energy. In Fig 9 and Fig 11, when displacement loading is adopted, the predicted uniaxial strengths are σ_2=-242.8 and τ_{12}=74.7 MPa; when force loading is adopted, the kinetic energy soars from σ_2=-248.0 MPa and τ_{12}=81.6 MPa, which are very close to the former ones. The uniaxial strength values from experiment are σ_2=-257 and τ_{12}=100 MPa [58], which means the RVE show a good accuracy for the strength prediction and specially the force loading method shows an even higher accuracy. Besides, the contours of equivalent plastic strains (PEEQ) for transverse compression and in-plane shear cases at the failure point in Fig 10 and Fig 12 show similar plastic strain distributions and shear bands. In addition, RVEs under σ_2 see a shear band at approximately 52º, which is in good agreement with [35]. Therefore, based on the findings from these two uniaxial loading cases, it can be concluded that the force loading method and displacement loading method for the RVE are almost equivalent in the transverse compression and in-plane shear loading cases with regard to failure identification, and similar conclusions also works for the meso-scale RVE of braided textile composites [59]. The failure points can be identified by analysing the kinetic curves and PEEQ contours when the RVE is applied with force loadings. In this study, following cases under biaxial and triaxial loads are applied by force loading.

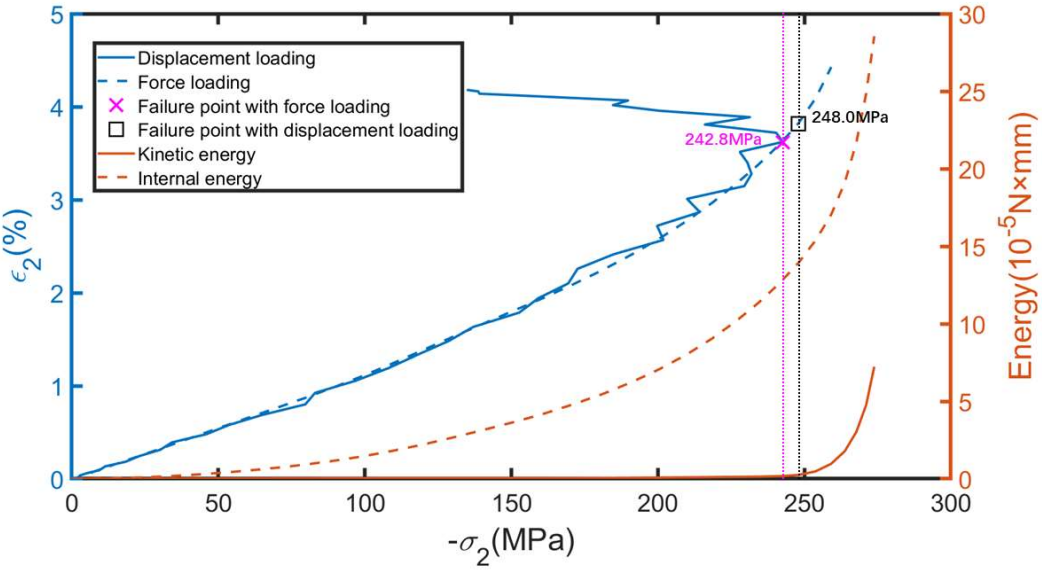

Fig 9. The strain-stress curve and energy for RVE under σ_2

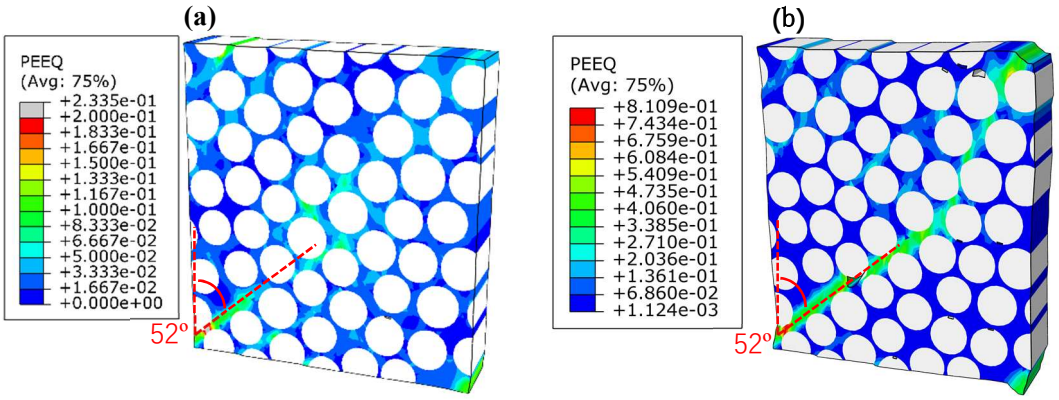

Fig 10. PEEQ for RVE at failure point under σ_2 realised by (a) displacement loading and (b) force loading.

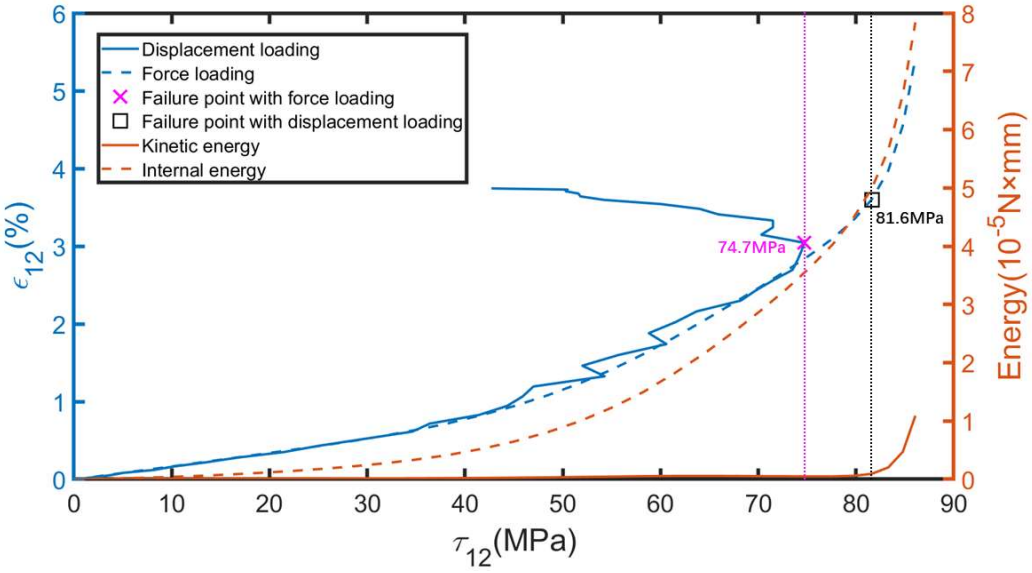

Fig 11. The strain-stress curve and energy for RVE under τ_{12}

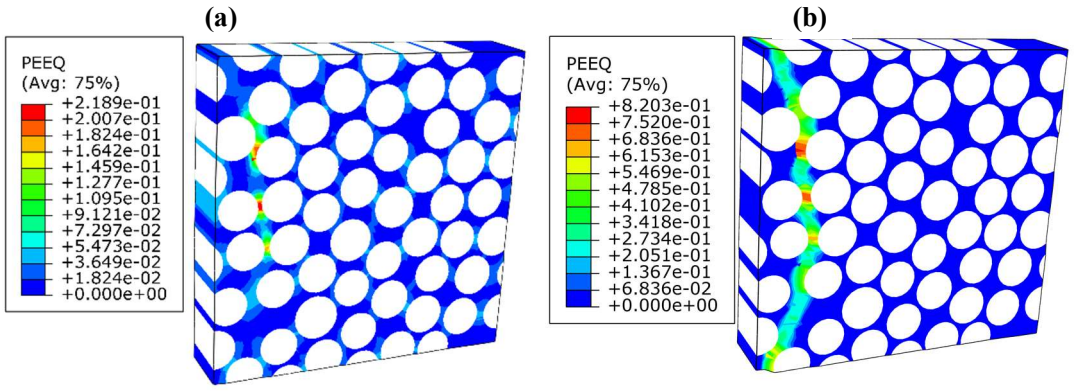

Fig 12. PEEQ for RVE at failure point under τ_{12} realised by (a) displacement loading and (b) force loading at failure point

4. Effects of loading path on the final failure under biaxial and triaxial loads

4.1 Effects of loading path on failure point under biaxial compression

Fig 13 shows the failure points obtained from the RVE subjected to biaxial compression, the transverse compression stress σ_2 and out-of-plane compression stress σ_3, with three different loading paths. In the radial path, the values of biaxial compression increase simultaneously, and the RVE fails at the point CC1 (σ_2=-419.5MPa, σ_3=-83.9MPa). In the orthogonal path, σ_3 increases to -83.9MPa in the first step and remains constant. Then in the second step σ_2 starts to increase until the failure of the RVE, where the failure occurs at the point CC2 (σ_2=-417.1MPa, σ_3=-83.9MPa). In the zigzag path, σ_3 increases to -160MPa in the first step to introduce extra plastic deformation, and then it reduces as σ_2 starts to increase simultaneously in the second step. The failure point of the RVE is at CC3 (σ_2=-439.9MPa, σ_3=-79.8MPa). These three failure points are very close to each other, with σ_2 having the largest difference of 5.5% (between CC2 and CC3).

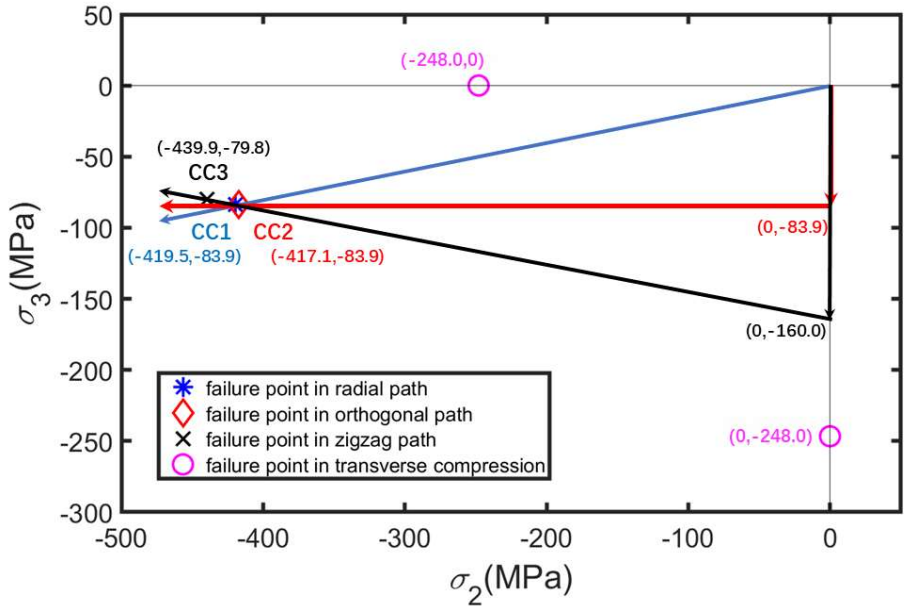

Fig 13. Three loading paths for the RVE under biaxial compression

In Fig 14, it is noticed that the PEEQ distributions of RVE with three different loading are very similar to each other. Besides, an interesting phenomenon observed from this case is that the compressive strength is significantly improved with all three loading paths under biaxial compression loading compared to the strength under transverse compression σ_2 or σ_3. This is because that the high stiffness of fibres leads to a high hydrostatic pressure in the matrix when the RVE is applied by biaxial compression. Before the failure occurs, the matrix and fibres are bonded by the interface, such that the strain of the matrix in fibre direction caused by Poisson effect is constrained by the interface. Due to the high stiffness of fibre and constraints of the interface, the strain of matrix in fibre direction is less than the strain caused by Poisson effect, which is manifested by the compressive stress in the matrix along the fibre direction (see Fig 15), resulting in a higher yielding strength and a higher failure strength.

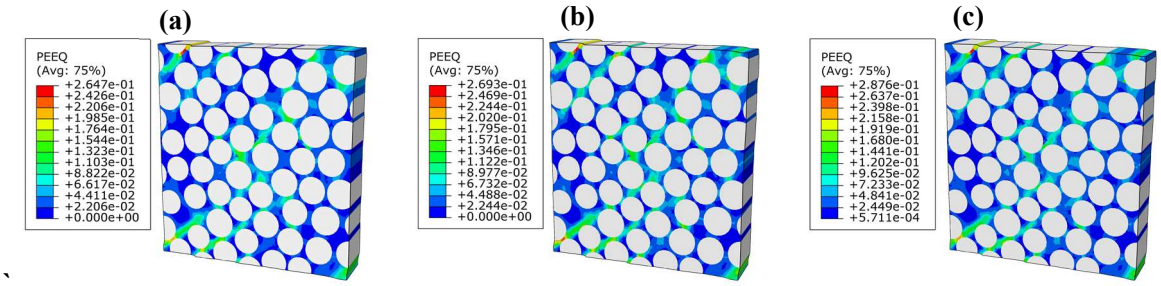

Fig 14. PEEQ for RVE at failure point under biaxial compression. (a) Radial path, (b) Orthogonal path, (c) Zigzag path.

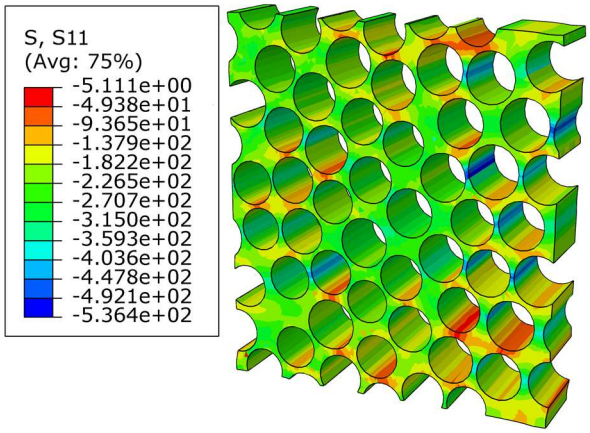

Fig 15. Normal stress in matrix along fibre direction for RVE at failure point under biaxial compression with radial path.

Three different loading paths for the RVE under σ_2 and τ_{12} with compression dominated failure are given in Fig 16. As can be seen, the failure points in three loading paths are in an excellent agreement, and the largest difference among these three failure points is 0.6% (between σ_2 of CS1C and σ_2 of CS3C). Fig 17 shows that the equivalent plastic distributions of the RVE at each failure point for three loading paths have a similar pattern. However, differences can still be observed in the zigzag loading path from the others as its maximum PEEQ is 11% larger than the other two cases, and the plastic strain in the fibre rich region is also slightly larger, which are due to the introduced extra plastic deformation.

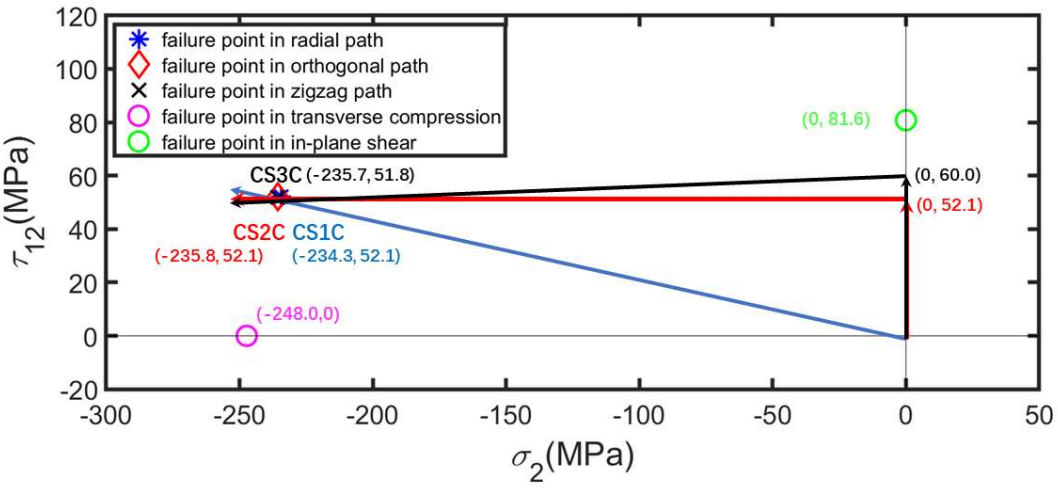

Fig 16. Compression dominated failure points for RVE under σ_2 and τ_{12} in three loading paths.

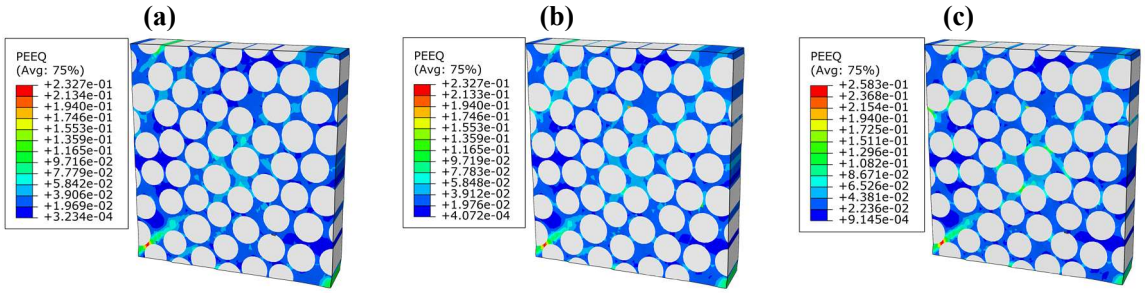

Fig 17. PEEQ for RVE at failure point under σ_2 and τ_{12} with compression dominated failure at the failure point. (a) Radial path, (b) Orthogonal path, (c) Zigzag path.

Fig 18 shows the comparison of the failure points obtained from the RVE subjected to σ_2 and τ_{12} with shear dominated failure using three different loading paths. Similarly, these three failure points are very close to each other, with the largest difference of 4.2% (between τ_{12} of C1SP1 and τ_{12} of C1SP3). Meanwhile, the three loading paths in this case show identical PEEQ distributions in Fig 19, and their failure patterns are similar to the one under in-plane shear in Fig 11, except the shear band being closer to the edge.

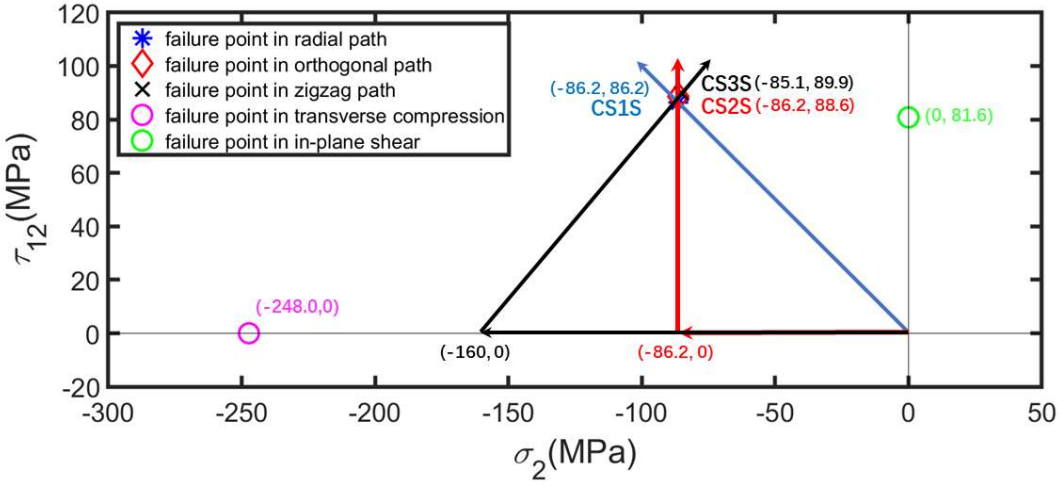

Fig 18. Shear dominated failure points for RVE under σ_2 and τ_{12} in three loading paths

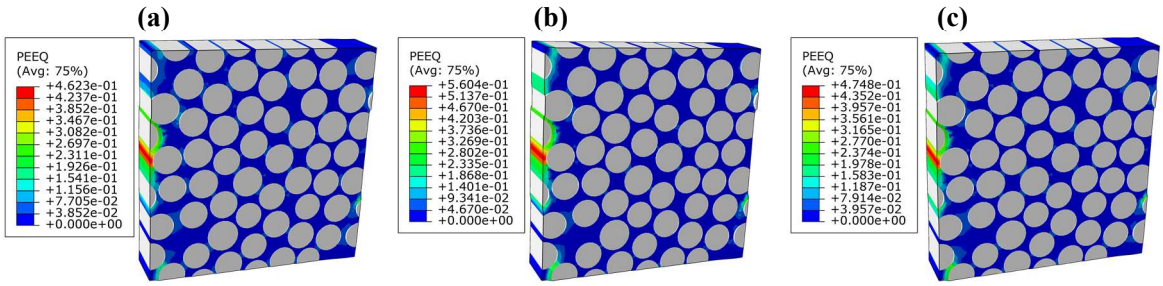

Fig 19. PEEQ for RVE at failure point under σ_2 and τ_{12} with shear dominated failure: (a) Radial path, (b) Orthogonal path and (c) Zigzag path.

4.2 Effects of loading path on failure point under triaxial loading

Fig 20 shows compression dominated failure points for the RVE under σ_2, σ_3 and τ_{12}. In the radial path, the absolute values of σ_2, σ_3 and τ_{12} are increased simultaneously, and the RVE fails at point CCS1C (σ_2=-390.0MPa, σ_3=-78.0MPa, τ_{12}=55.8MPa). In the orthogonal path, σ_3 increase to -78.0 MPa in the first step and reduces as τ_{12} starts to load until reaching 55.8 MPa; then σ_2 starts to load in the third step until the RVE fails at CCS2C (σ_2=-400.0 MPa, σ_3=-78.0 MPa, τ_{12}=55.8 MPa). In the zigzag path, σ_3 increases to -160MPa in the first step to introduce extra plastic deformation and reduces to -78.0MPa as τ_{12} starts loading until reaching 66.0MPa in the second step to introduce extra plastic deformation; then τ_{12} reduces and σ_2 starts to load in the third step; the RVE fails at CCS3C (σ_2=-377.2MPa, σ_3=-78.0MPa, τ_{12}=56.1MPa). These three failure points are very close to each other with the largest difference of 5.7% (between σ_2 of CCS2C and σ_2 of CCS3C). The PEEQ distributions of RVE for three loading path shown Fig 21 are also identical to each other, and their failure pattern are similar to the one under σ_2 in Fig 14.

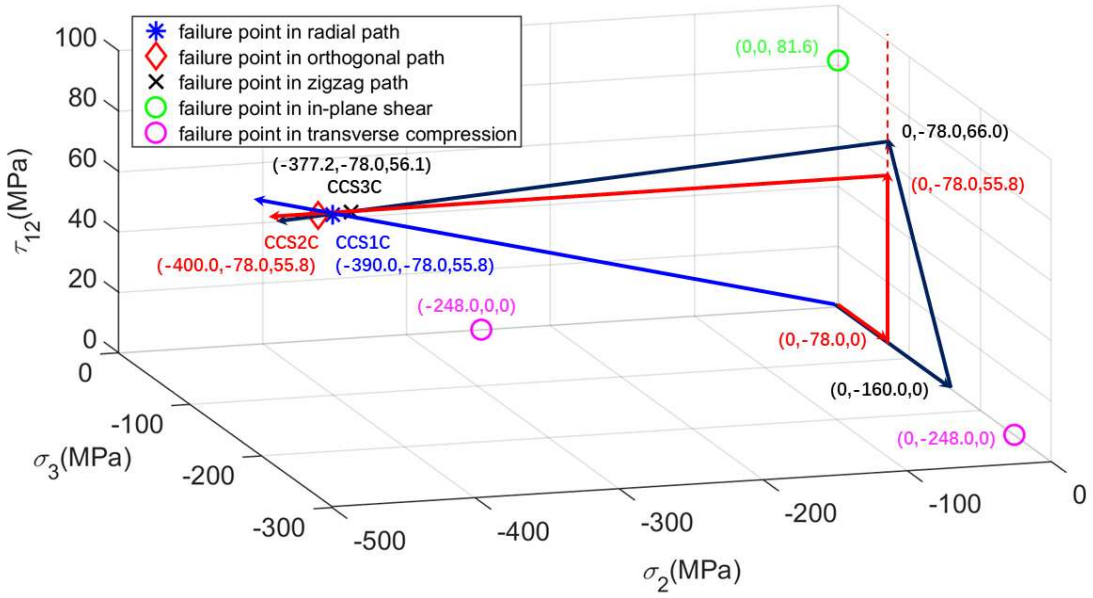

Fig 20. Compression dominated failure points for RVE under σ_2, σ_3 and τ_{12} in three loading paths

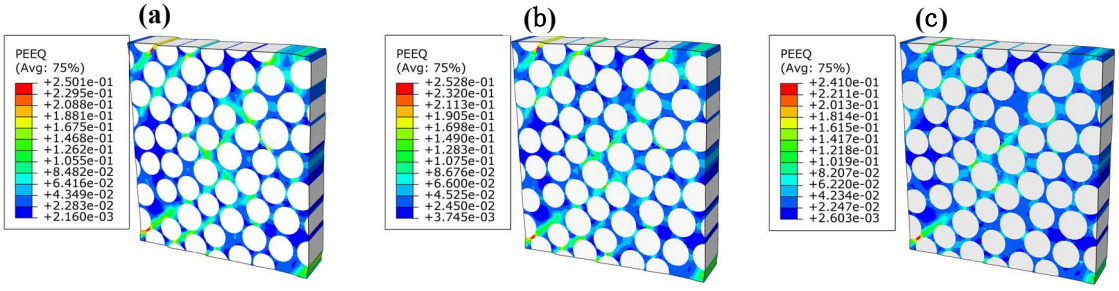

Fig 21. PEEQ for RVE at failure point under σ_2, σ_2 and τ_{12} with compression dominated failure: (a) Radial path, (b) Orthogonal path and (c) Zigzag path.

In Fig 22, three different loading paths for the RVE with shear dominated failure under σ_2, σ_3 and τ_{12} are given. Apparently, three failure points are very close, with the largest difference of 2.9% (between

τ_{12} of CCS1S and τ_{12} of CCS3S). The PEEQ distributions in Fig 23 are also identical, and the failure patterns are similar to the RVE with in-plane shear as shown in Fig 19.

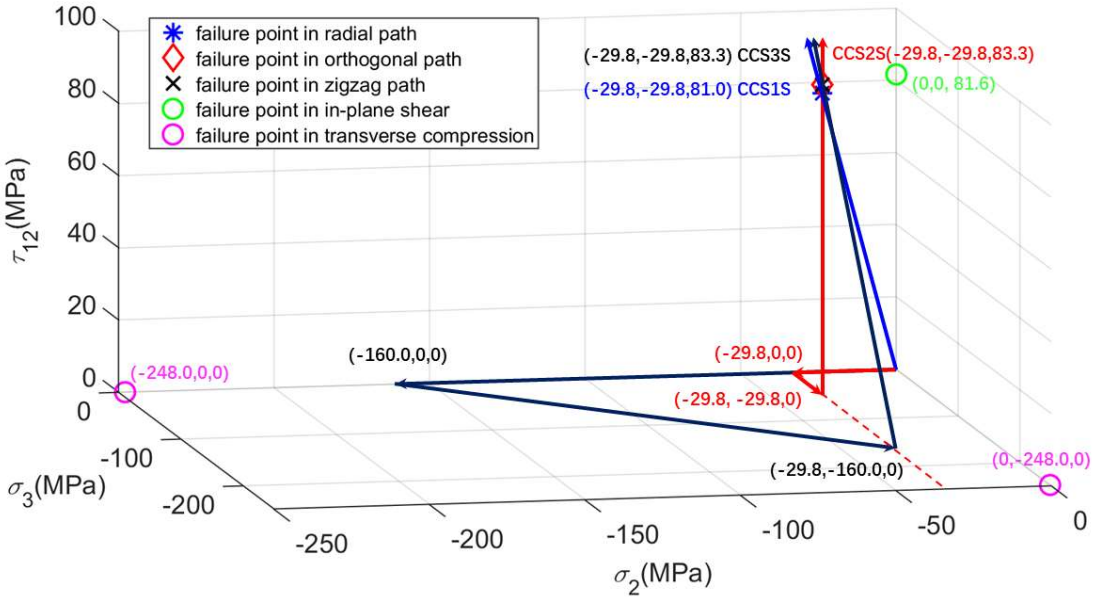

Fig 22. Shear dominated failure points for RVE under σ_2, σ_2 and τ_{12} in three loading paths.

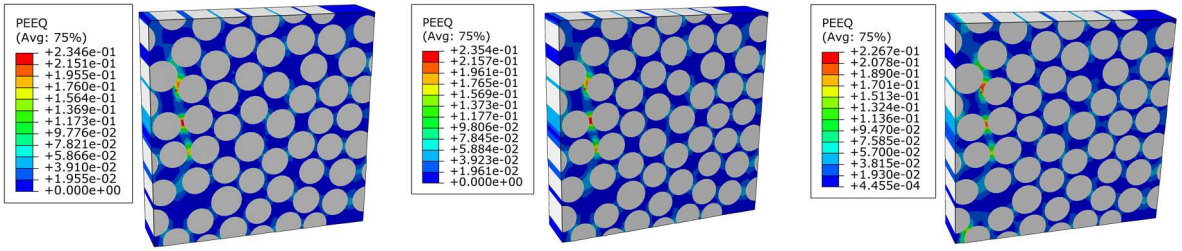

Fig 23. PEEQ for RVE at failure point under σ_2, σ_2 and τ_{12} with shear dominated failure: (a) Radial path, (b) Orthogonal path and (c) Zigzag path.

To sum up, the failure strengths and failure patterns at the failure point for RVE under the above loading cases are very close for all three different loading paths. It is surprising that even the zigzag path, introducing extra plastic deformation in the RVE, show a negligible difference in the predicted failure strength. This implies that the failure in composite is more related to the plastic deformation in the direction that failure happens. For example, in Fig 20, the failure happens in the direction of ε_2, and the zigzag path introduces extra plastic deformation in ε_3 and ε_{12}, so the failure point in zigzag path is identical to other two paths. The same happen in all other cases.

5. Conclusions

In this paper, the influence of three different loading paths on the failure strength and failure pattern of the UD CFRP composite laminae under combined transverse compression, out-of-plane compression and in-plane shear is studied. This is achieved by means of a 3D RVE FE model based on the UD lamina microstructure. The RVE includes the fibre, matrix and interface to capture the mechanical behaviour

of each constituent and an elastoplastic constitutive model, modified Drucker-Prager plastic damage model, is used to capture the mechanical response of RVE.

Three different loading paths are compared, including the radial path, the orthogonal path and the zigzag path which introduces extra plastic deformation. In order to control the loading path precisely, the force loading method, instead of the commonly-used displacement loading method, is used in RVE. Such that the failure of the RVE can be identified from the monitoring of kinetic energy. The force loading method and displacement loading method are compared in transverse compression and in-plane shear cases, which shows that both are equivalent in failure determination. Afterward, three loading paths are compared in biaxial loading cases and triaxial loading cases. The results suggest that the three loading paths show negligible effects on the final failure strength and the failure pattern of UD composite laminae under combined transverse compression, out-of-plane compression and in-plane shear loading. The main advantage of this approach is that the high-fidelity FE model consists of three phases, including fibres, matrix and non-zero thickness interface, in which the matrix is modelled as an isotropic elasto-plastic solid considering the influence of hydrostatic stress. On the other hand, the fibre/matrix interface properties (stiffness and thickness) which are difficult to be measured by experiments are identified by artificial neural network (ANN), rather than simply using the empirical values.

Together with the previous findings in literature [11,18,25,33] for other biaxial loading cases, it therefore suggests that it is reasonable to use the failure criteria without considering the loading path to assess the matrix dominated failure of UD composite laminae. Although this paper draws the same conclusion as these previous works, some substantial improvements have been achieved. First, a high-fidelity FE model was established with three phases, i.e., fibres, matrix and non-zero thickness interface, in which the experimentally difficult-to-measure parameters are identified with artificial neural network. Second, it extended the previous works, which only consider combined transverse and in-plane shear loadings, into biaxial compression cases and triaxial loadings cases that are common, real service loading conditions. In addition, it applied a force loading approach instead of the displacement loading to precisely control the loading path, allowing the realisation of any kind of loading paths. Finally, it introduced extra plastic deformation to study its influences on the failure of composites.

Acknowledgement

The first two authors (JC and LW) would like to thank China Scholarship Council (CSC) for sponsoring their studies.

References

[1] Mouritz AP, Gellert E, Burchill P, Challis K. Review of advanced composite structures for naval ships and submarines. Compos Struct 2001;53:21–42.

[2] Egbo MK. A fundamental review on composite materials and some of their applications in biomedical engineering. J King Saud Univ - Eng Sci 2020.

[3] Hollaway LC. A review of the present and future utilisation of FRP composites in the civil infrastructure with reference to their important in-service properties. Constr Build Mater 2010;24:2419–45.

[4] Bradshaw RD. Modified Tsai-Wu Failure Criterion 1992:273–7.

[5] Christensen R. Failure Criteria for Anisotropic Fiber Composite Materials. FailurecriteriaCom 2008.

[6] Yeh HL, Yeh HY. The modified quadric surfaces criterion for composite materials. J Reinf Plast Compos 2002;21:277–89.

[7] Liu KS, Tsai SW. A progressive quadratic failure criterion for a laminate. Fail Criteria Fibre-Reinforced-Polymer Compos 2004;3538:334–52.

[8] Puck A, Schürmann H. FAILURE ANALYSIS OF FRP LAMINATES BY MEANS OF PHYSICALLY BASED PHENOMENOLOGICAL MODELS. Compos Sci Technol 1998;58:1045–67.

[9] Kaddour AS, Hinton MJ. Maturity of 3D failure criteria for fibre-reinforced composites: Comparison between theories and experiments: Part B of WWFE-II. J Compos Mater 2013;47:925–66.

[10] Tsai SW, wu EM. A General Theory of Strength for Anisotropic Materials. J Compos Mater. 1971;5:58–80.

[11] Totry E, González C, Llorca J. Influence of the Loading Path on the Strength of Fiber-Reinforced Composites Subjected to Transverse Compression and Shear. Int J Solids Struct 2008;45.

[12] Kaddour AS, Hinton MJ. Input data for test cases used in benchmarking triaxial failure theories of composites. J Compos Mater 2012;46:2295–312.

[13] Talreja R. Physical modelling of failure in composites. Philos Trans R Soc A Math Phys Eng Sci. 2016;374:20150280.

[14] Bing Q, Sun CT. Specimen size effect in off-axis compression tests of fiber composites. Compos Part B-Engineering - Compos PART B-ENG 2008;39:20–6.

[15] Nemeth M, Herakovich C, Post D. On the Off-Axis Tension Test for Unidirectional Composites. J Compos Technol Res 1982;5.

[16] Danila AN, Steigmann R, Savin A, Blanari I, Barsanescu PD. Arcan device employed in CFRP testing. 10th Int Work NDT Prog 2019.

[17] Cognard JY, Sohier L, Davies P. A modified Arcan test to analyze the behavior of composites and their assemblies under out-of-plane loadings. Compos Part A Appl Sci Manuf 2011;42:111–21.

[18] Choo VKS. Effect of Loading Path on the Failure of Fibre Reinforced Composite Tubes. J Compos Mater 1985;19:525–32.

[19] Hannon A, Tiernan P. A review of planar biaxial tensile test systems for sheet metal. J Mater Process Technol 2008;198:1–13.

[20] Welsh JS, Adams DF. Development of an electromechanical triaxial test facility for composite materials. Exp Mech. 2000;40:312–20.

[21] Shin ES, Pae KD. Effects of Hydrostatic Pressure on the Torsional Shear Behavior of Graphite/Epoxy Composites. J Compos Mater. 1992;26:462–85.

[22] Shin ES, Pae KD. Effects of Hydrostatic Pressure on In-Plane Shear Properties of Graphite/Epoxy Composites. J Compos Mater. 1992;26:828–68.

[23] Zinoviev PA, Tsvetkov S V., Kulish GG, Van Den Berg RW, Van Schepdael LJMM. The behavior of high-strength unidirectional composites under tension with superposed hydrostatic pressure. Compos Sci Technol 2001;61:1151–61.

[24] Zinoviev P, Tsvetkov S. Mechanical behavior of high strength unidirectional composites under 3-D state of stress. Iccm12 1999.

[25] Vogler TJ, Kyriakides S. Inelastic behavior of an AS4/PEEK composite under combined transverse compression and shear. Part I: experiments. Int J Plast 1999;15:783–806.

[26] Gitman I, Askes H, Sluys L, Lloberas-Valls O. The concept of Representative Volume for elastic, hardening and softening materials. 2004.

[27] Moes N, Dolbow J, Belytschko T. A finite element method for crack growth without remeshing. Int J Numer Meth Eng 1999;46:131–50.

[28] Karihaloo BL, Xiao QZ. Modelling of stationary and growing cracks in FE framework without remeshing: a state-of-the-art review. Comput Struct 2003;81:119–29.

[29] Zhang P, Hu X, Bui T Q, et al. Phase field modeling of fracture in fiber reinforced composite laminate. International Journal of Mechanical Sciences, 2019, 161-162: 105008.

[30] Zhang P, Feng Y, Bui T Q, et al. Modelling distinct failure mechanisms in composite materials by a combined phase field method. Compos Struct, 2020, 232: 111551.

[31] Zhang P, Yao W, Hu X, et al. 3D micromechanical progressive failure simulation for fiber-reinforced composites. Compos Struct, 2020, 249: 112534.

[32] Zhang P, Yao W, Hu X, et al. An explicit phase field model for progressive tensile failure of composites. Eng Fract Mech, 2021, 241: 107371.

[33] Sun Q, Zhou G, Meng Z, Guo H, Chen Z, Liu H, et al. Failure criteria of unidirectional carbon fiber reinforced polymer composites informed by a computational micromechanics model. Compos Sci Technol 2019;172:81–95.

[34] Kanit T, Forest S, Galliet I, Mounoury V, Jeulin D. Determination of the size of the representative volume element for random composites: statistical and numerical approach. Int J Solids Struct. 2003;40:3647–79.

[35] González C, LLorca J. Mechanical behavior of unidirectional fiber-reinforced polymers under transverse compression: Microscopic mechanisms and modeling. Compos Sci Technol, 2007;67:2795–806.

[36] Soden PD, Hinton MJ, Kaddour AS. Lamina properties, lay-up configurations and loading conditions for a range of fibre-reinforced composite laminates. Compos Sci Technol, 1998;58:1011–22.

[37] Ismail Y, Yang D, Ye J. Discrete element method for generating random fibre distributions in micromechanical models of fibre reinforced composite laminates. Compos Part B Eng, 2016;90:485–92.

[38] Alfano G, Sacco E. Combining interface damage and friction in a cohesive-zone model. Int J Numer Methods Eng. 2006;68(5):542–82.

[39] Van Der Meer FP, Sluys LJ. A numerical investigation into the size effect in the transverse crack tension test for mode II delamination. Compos Part A Appl Sci Manuf, 2013;54:145–52.

[40] Chevalier J, Camanho PP, Lani F, Pardoen T. Multi-scale characterization and modelling of the transverse compression response of unidirectional carbon fiber reinforced epoxy. Compos Struct, 2019;209:160–76.

[41] Turon A, González EV, Sarrado C, Guillamet G, Maimí P. Accurate simulation of delamination under mixed-mode loading using a cohesive model with a mode- dependent penalty stiffness. Compos Struct, 2017;184:506–11.

[42] Ward IM. Review: The yield behaviour of polymers. J Mater Sci, 1971;6:1397–417.

[43] Fiedler B, Hojo M, Ochiai S, Schulte K, Ando M. Failure behavior of an epoxy matrix under different kinds of static loading. Compos Sci Technol, 2001;61:1615–24.

[44] Wan L, Ismail Y, Zhu C, Zhu P, Sheng Y, Liu J, et al. Computational micromechanics-based prediction of the failure of unidirectional composite lamina subjected to transverse and in-plane shear stress states. J Compos Mater, 2020;54:3637–54.

[45] Naya F, González C, Lopes CS, Van der Veen S, Pons F. Computational micromechanics of the transverse and shear behavior of unidirectional fiber reinforced polymers including environmental effects. Compos Part A Appl Sci Manuf, 2017;92:146–57.

[46] Melro AR, Camanho P, Andrade Pires F, Pinho S. Micromechanical analysis of polymer composites reinforced by unidirectional fibres: Part I – Constitutive modelling. Int J Solids Struct, 2013;50:1897–1905.

[47] Lubliner J, Oliver J, Oller S, Oñate E. A plastic-damage model for concrete. Int J Solids Struct. 1989;25:299–326.

[48] Jeeho L, L. FG. Plastic-Damage Model for Cyclic Loading of Concrete Structures. J Eng Mech, 1998;124:892–900.

[49] De Moura M, Gonçalves J, Marques A, et al. Modeling compression failure after low velocity impact on laminated composites using interface elements. J Compos Mater, 1997, 31(15): 1462-79.

[50] Dourado N, Moura MFSFD, Morais ABD, et al. Bilinear approximations to the mode II delamination cohesive law using an inverse method. Mechanics of Materials, 2012, 49: 42-50.

[51] Varna, J., Berglund, L., Ericson, M., 1997. Transverse single-fibre test for interfacial debonding in composites: Modelling. Compos Part A-Appl S, 28, 317–326.

[52] Sharma A, Daggumati S, Gupta A, Van Paepegem W. On the prediction of the bi-axial failure envelope of a UD CFRP composite lamina using computational micromechanics: Effect of microscale parameters on macroscale stress–strain behavior. Compos Struct 2020;251:112605.

[53] Yaser I, Lei W, Jianqiao Y, Dongmin Y. An ABAQUS® plug-in for generating virtual data required for inverse analysis of unidirectional composites using artificial neural networks. Compos Struct (under review).

[54] Dozat T. Incorporating Nesterov momentum into Adam, in: Proceedings of the International Conference on Learning Representation, 2018.

[55] Koerber H. Mechanical Response of Advanced Composites under High Strain Rates 2010:262.

[56] Garoz D, Gilabert FA, Sevenois RDB, Spronk SWF, Van Paepegem W. Consistent application of periodic boundary conditions in implicit and explicit finite element simulations of damage in composites. Compos Part B Eng 2019;168:254–66.

[57] Zhang C, Curiel-Sosa J L, Bui T Q. Comparison of periodic mesh and free mesh on the mechanical properties prediction of 3D braided composites. Compos Struct, 2017, 159: 667-76.

[58] Koerber H, Xavier J, Camanho PP. High strain rate characterisation of unidirectional carbon epoxy IM7-8552 in transverse compression and in-plane shear using digital image correlation. Mech Mater, 2010, 1004-19.

[59] Zhang C, Mao C, Curiel-Sosa J L, et al. Meso-Scale Finite Element Simulations of 3D Braided Textile Composites: Effects of Force Loading Modes. Appl Compos Mater, 2018, 25(4): 823-41.